Channel characteristics and transmission performance for various channel configurations at 60 GHz

Hindawi Publishing Corporation
EURASIP Journal on Wireless Communications and Networking
Volume 2007, Article ID 19613, 15 pages
doi:10.1155/2007/19613

Research Article

Channel Characteristics and Transmission Performance for Various Channel Configurations at 60 GHz

Haibing Yang, Peter F. M. Smulders, and Matti H. A. J. Herben

Department of Electrical Engineering, Eindhoven University of Technology, P.O. Box 513, 5600 MB Eindhoven, The Netherlands

Received 13 June 2006; Accepted 20 March 2007

Recommended by Chia-Chin Chong

Extensive measurements are conducted in room environments at 60 GHz to analyze the channel characteristics for various channel configurations. Channel parameters retrieved from measurements are presented and analyzed based on generic channel models. Particularly, a simple single-cluster model is applied for the parameter retrieval and performance evaluation. By this model, power delay profiles are simply described by a K-factor, a root-mean-squared delay spread, and a shape parameter. The considered channels are configured with the combination of omnidirectional, fan-beam, and pencil-beam antennas at transmitter and receiver sides. Both line-of-sight (LOS) and non-LOS (NLOS) channels are considered. Further, to evaluate the transmission performance, we analyze the link budget in the considered environments, then design and simulate an OFDM system with a data rate of 2 Gbps to compare the bit-error-rate (BER) performance by using the measured and modeled channels. Both coded and uncoded OFDM systems are simulated. It is observed that the BER performance agrees well for the measured and modeled channels. In addition, directive configurations can provide sufficient link margins and BER performance for high data rate communications. To increase the coverage and performance in the NLOS area, it is preferable to apply directive antennas.

1. INTRODUCTION

In recent years, intensive efforts have been made worldwide for the application of high data rate wireless communication system in the frequency band of 60 GHz [1–5]. Special features of the radio propagation in this frequency band, namely high penetration loss of construction materials and severe oxygen absorption, and broadband spectrum (common bands of 59–62 GHz worldwide) make it suitable for the deployment of high data rate short-distance communications [3, 6]. Recently, the IEEE 802.15.3 Task Group 3c was formed to standardize the 60 GHz wireless personal area network (WPAN) systems, which will allow high data rate up to 3 Gbps [5]. Even higher data rate requirements would be expected in the future. The low-cost and low-complexity implementation of such systems requires a suitable channel model for the characteristics of the 60 GHz radio propagation, which can be used for the codesign of RF front-end and baseband processing. To this end, this paper will focus on channel modelling, model parameter retrieval, and system performance evaluation over 60 GHz channels.

One of the biggest challenges for designing a high data-rate 60 GHz system is the limited link budget due to high path loss during radio propagation [3, 5–7]. For a fixed separation between transmitter (TX) and receiver (RX), the propagation loss at 60 GHz is about 30 dB higher than at 2 GHz in free space. In this sense, it is preferable to employ high-gain directive antennas, especially for a fixed point-to-point application. Thanks to the relatively small dimensions of 60 GHz antennas, an alternative to high-gain antennas is to use highly flexible antenna arrays for adaptive beamforming. On the other hand, an omnidirectional antenna might be used in some applications where a full coverage is required.

For most 60 GHz applications, the transmitter and the receiver will keep stationary, and the time variation of the channel will be introduced by moving objects due to the Doppler effect. In particular, the movements of human bodies within the channel will cause significant temporal fading and shadowing effect, whose level depends on the moving speed, the number of persons, and the propagation environment [8–10]. The remaining significant impact on the system caused by the radio channel is the frequency selectivity due

to multipath effect, which induces intersymbol interference (ISI) in communication systems [11–14].

Multipath propagation in indoor environments is strongly affected by the dimensions of the environment and the density of furnishings. The influence of the environment on the channel can be noticed in the power delay profile (PDP), which describes the span of the received signal over time delay. In a local area within a range of tens of wavelength, cluster-wise arrival behavior of scattered waves has been observed from measurements and the average PDP is formulated by multicluster models [15–19]. In a global area such as a room environment, the average PDP is exponentially decaying over delay in addition to the direct path [20, 21]. In this single cluster model, a constant-level part might appear before the decaying part caused by the elevation dependence of antenna radiation patterns and the height difference between the transmit antenna and the receive antenna [21]. The impact of various PDP shapes on system performance has been considered in [12, 22, 23]. There they conclude that as long as the root-mean-squared (RMS) delay spread of the PDP is small compared with the symbol duration, the profile shape has a negligible impact on system performance, but the performance is strongly influenced by the RMS delay spread.

The purpose of this paper is to analyze the 60 GHz channel characteristics and to evaluate the system performance for various channel configurations. Due to the simplicity and the directness of the relationship between RMS delay spread (RDS) and PDP, the simple single-cluster model is applied to retrieve model parameters from measurements and used to evaluate the system performance. The structure of this paper is as follows. In Section 2, we give an overview of the generic theory for radio channels. In Section 3, channel measurements will be described in indoor environments for various antenna configurations. Then, channel parameters are retrieved and analyzed from the measured data. Particularly, the shape parameters of power delay profiles are retrieved to distinguish the channel characteristics of various configurations. Next in Section 4, we analyze the link budget and then simulate an equivalent baseband OFDM system for 60 GHz radio applications. The coded/uncoded BER performance is evaluated and compared for the measured and modeled channels. The BER performance for various channel configurations is also analyzed. Finally, conclusions are given in Section 5.

2. INDOOR CHANNEL THEORY

In a typical indoor radio environment, over a distance of as short as half a wavelength, the magnitude of the received signal will be subject to a rapid variation by as much as tens of dBs. This variation of the received signal is called channel fading and is caused by the propagation of multipath waves in addition to the line-of-sight (LOS) wave. For the 60 GHz radio applications in indoor environments, it is highly likely that the receiver can only be used within a single room, for example, an open office, where the transmitter is located, due to high penetration loss caused by its construction materials. In this case, the multipath waves are mainly the reflected or scattered waves from main objects such as the walls, furniture, the floor, the ceiling. In a local area, the rapid variation of the received signal envelope is called small-scale fading and can be characterized by a Rician distribution [1, 13, 24]. When there is no contribution from a specular path such as the LOS path, the fading becomes Rayleigh distributed. The local mean of the received signal also varies over distance but much less rapidly. This slower variation is caused by the furnishing and the structure of the room environment. When measured over distances of several hundred wavelengths, the slow variation is called large-scale fading that is highly dependent on the distance. The large-scale variation can be empirically characterized by two multiplicative terms: an exponentially decaying term over distance and a log-normal distributed term with the standard deviation highly dependent on the environment [1, 13, 25].

For a wideband transmission system, the complex lowpass impulse response of a Rician channel is modeled as a direct or strong specular path plus N independent Rayleigh fading paths and can be expressed by[1]

$$h(t,\tau) = \alpha_0 e^{j\phi_0(t)}\delta(\tau-\tau_0) + \sum_{n=1}^{N} \alpha_n e^{j\phi_n(t)}\delta(\tau-\tau_n), \quad (1)$$

where $\alpha_0 e^{j\phi_0(t)}$ is the response of the direct or strong specular path which stays stationary in a local area, $\{N, \alpha_n, \phi_n, \tau_n\}$ are randomly time-varying variables: the number of multiple paths, the amplitude, phase, and arrival-time of the nth path, respectively. The time dependency of the channel is introduced by arbitrary movements of the transmitter, the receiver or other objects. Since the path number, the amplitude and the arrival-time are relatively static in a local area, the time dependency is omitted here. A Rician K-factor is usually used to characterize the Rician fading channel and defined as the ratio between the powers contributed by the steady path and the scattered paths, that is,

$$K = \frac{E\{|\alpha_0|^2\}}{2\sigma^2}, \quad (2)$$

where $2\sigma^2$ is the mean power of the scattered paths.

For physical channels, it is reasonable to assume that the channel statistic is stationary or quasistatic, that is, wide-sense stationary (WSS), within the time duration of one transmitted symbol or one data package. Moreover, signals coming via different paths will experience uncorrelated attenuations, phase shifts, and time delays, which is referred to as uncorrelated scattering (US). The assumption of WSSUS for physical channels has been experimentally confirmed and widely accepted in literature [9, 13, 24, 27–29]. Under the WSSUS assumption, the autocorrelation of the complex

[1] The assumption of Rayleigh fading for the nonspecular paths is supported by the indoor channel measurements given in [24, 26].

impulse response $h(t,\tau)$ will be only dependent on the time difference and satisfies

$$\phi_h(\Delta t;\tau_1,\tau_2) = \frac{E\{h^*(t,\tau_1)h(t+\Delta t,\tau_2)\}}{\sqrt{E\{|h^*(t,\tau_1)|^2\}E\{|h(t+\Delta t,\tau_2)|^2\}}} = \phi_h(\Delta t,\tau_1)\delta(\tau_2-\tau_1). \tag{3}$$

Furthermore, the average power delay profile of the channel is defined as the autocorrelation function when $\Delta t = 0$,

$$P(\tau) = E\{|h(t,\tau)|^2\} = \sum_{n=0}^{N} E\{|\alpha_n|^2\}\delta(\tau-\tau_n) \tag{4}$$

which is the average of instantaneous power delay profiles in a local area. From the average power delay profile, the RDS σ_s can be defined by

$$\sigma_s = \sqrt{\sum_{n=0}^{N} P(\tau_n)(\tau_n-\overline{\tau})^2} \tag{5}$$

with the mean excess delay $\overline{\tau} = \sum_{n=0}^{N}\tau_n P(\tau_n)$, where it is assumed that $\sum_{n=0}^{N} E\{|\alpha_n|^2\} = 1$. RDS is generally used to characterize the time dispersion of the channel.

The equivalent complex channel frequency response $H(t,f)$ is written as

$$H(t,f) = \sum_{n=0}^{N} \alpha_n e^{j(\phi_n(t)-2\pi\tau_n f)} \tag{6}$$

which is the Fourier transform of (1) over τ. Under the WSSUS assumption, it can be shown that the frequency autocorrelation function of $H(t,f)$ does not depend on the specific frequency and can be written as

$$\phi_H(\Delta t;f_1,f_2) = \frac{E\{H^*(t,f_1)H(t+\Delta t,f_2)\}}{\sqrt{E\{|H^*(t,f_1)|^2\}E\{|H(t+\Delta t,f_2)|^2\}}} = \phi_H(\Delta t,\Delta f) \tag{7}$$

with $\Delta f = f_2 - f_1$, where $\phi_H(\Delta t,f)$ is the Fourier transform of $\phi_h(\Delta t,\tau)$. For $\Delta t = 0$, the resulting $\phi_H(\Delta f) \doteq \phi_H(0,\Delta f)$ represents the channel coherence level over the frequency separation Δf. The coherence bandwidth B_c is defined as the largest frequency separation over which the correlation $|\phi_H(\Delta f)|$ is not smaller than a level, for example, 0.5 or 0.9. The coherence bandwidth is a statistical measure in characterizing the frequency selectivity of a channel.

The transmission channel can vary over time due to Doppler effect caused by moving objects or moving antennas at the transmitter or receiver side, which results in a spectrum broadening. Compared to the dramatic phase change caused by Doppler effect, the amplitude and the incident angles stay quasistationary. When the receiver is moving at speed v, the phase of the nth path is generally modeled by [30, 31]

$$\phi_n(t) = \overline{\phi}_n + 2\pi\frac{f_c v}{c}t\cos\theta_n, \tag{8}$$

where $\overline{\phi}_n$ is the phase when the channel is static, f_c the carrier frequency, c the speed of light, and θ_n the angle between the moving direction and the incident direction. When the angles of arrival of the multipath components are uniformly distributed in all the directions in a horizontal plane, a "U"-shape Doppler spectrum, that is well known as the classic 2D Clarke's model, will appear [30, 31]. When a specular path exists in the channel, a spike will appear in the Doppler spectrum. The 2D model can be further extended to 3D models [32, 33], which might be suitable for indoor wave propagations.

For most applications of indoor 60 GHz radio systems, the transmitter and receiver are stationary and the time variations of the channel are actually caused by moving objects. Then, the phase of the nth path reflected at a moving object with the speed v becomes [34]

$$\phi_n(t) = \overline{\phi}_n + 4\pi\frac{f_c v}{c}t\cos\theta_n\cos\varphi_n, \tag{9}$$

where θ_n is the reflection angle of the path at the moving object and φ_n the angle between the direction of movement and the direction orthogonal to the reflecting surface. In a similar way, the Doppler shift caused by multiple moving objects can be expressed. The resulting Doppler spectrum will show a "bell" shape, which has been observed from measurements [8, 9, 28].

Proportional to the carrier frequency, the Doppler effects at 60 GHz are relatively severe. For instance, a moving object at a speed of 2 m/s can lead to a Doppler spread as large as 1.6 kHz. For a fixed application, Doppler effects caused by moving objects can be significantly reduced by employing directive antennas or smart antenna technologies, as long as the signal path is not blocked by objects. But for directive configurations, once the direct path is blocked by moving objects, the communication link can be completely lost [8, 35].

3. CHANNEL MEASUREMENTS AND ANALYSIS

In this section, statistical channel parameters are retrieved from channel measurements conducted in room environments and analyzed for various antenna configurations.

3.1. Description of environment and measurements

An HP 8510C vector network analyzer was employed to measure complex channel frequency responses. During measurement, the step sweep mode was used and the sweep time of each measurement was about 20 seconds. Channel impulse responses were obtained by Fourier transforming the frequency responses into time domain after a Kaiser window was applied with a sidelobe level of −44 dB. Three types of vertical polarized antennas with different radiative patterns, that is, omnidirectional, fan-beam, and pencil-beam antennas, were applied in our measurements. Parameters of these antennas, half power beamwidth (HPBW), and antenna gain, are listed in Table 1.

Two groups of measurements were conducted in room A and B separately on the 11th floor of the PT-building at

Table 1: Antenna parameters.

Type of antennas	Half power beamwidth (◦)		Gain (dBi)
	E-plane	H-plane	
Fan beam	12.0	70.0	16.5
Pencil beam	8.3	8.3	24.4
Omnidirectional	9.0	Omnidirectional	6.5

Eindhoven University of Technology. The plan view of the rooms are given in Figure 1. The dimensions of the rooms are $11.2 \times 6.0 \times 3.2\,\text{m}^3$ and $7.2 \times 6.0 \times 3.2\,\text{m}^3$, respectively. Both rooms have a similar structure. The windows side consists of window glasses with a metallic frame one meter above the floor and a metallic heating radiator below the window. The concrete walls are smoothly plastered and the concrete floor is covered with linoleum. The ceiling consists of aluminium plates and light holders. Some large metallic objects, such as cabinets, were standing on the ground. Note that in room A, three aligned metallic cabinets are standing in the middle of the room and two metallic cable boxes with a height of 3.2 m are attached to the brick wall side 2. The space between cabinets and ceiling has been blocked by aluminum foil for the ease of the measurement analysis.

Table 2 lists the measurement system configurations and scenarios. In room A, at both the transmitter and the receiver side, we use the same type of omnidirectional antennas. Three height differences of TX-RX were considered, namely, 0.0, 0.5, and 1.0 m (denoted by $\text{OO}_{0.0}$, $\text{OO}_{0.5}$, and $\text{OO}_{1.0}$ for three cases, resp.). Both LOS and non-LOS (NLOS) channels were measured in room A. In room B, a sectoral horn antenna with fan-beam pattern was applied at the TX side and located in a corner of the room at the height of 2.5 m. At the RX side, we used three types of antennas with omnidirectional, fan-beam, and pencil-beam patterns at the height of 1.4 m. The three TX/RX combinations are denoted by FO, FF, and FP, respectively, in which of the latter two cases the TX/RX beams are directed towards each other. In addition, we measured the channels for the cases of FF and FP with TX/RX beams misaligned by ±35° (denoted by $\text{FF}_{\pm 35^\circ}$ and $\text{FP}_{\pm 35^\circ}$). In room B, only LOS channels were measured.

During measurement, the transmitter and receiver were kept stationary and there were no movement of persons in the rooms.

3.2. Received power

The received power from a transmitter at a separation distance d is related to the path loss and can be represented by

$$P_r(d) = P_t + G_t + G_r - \text{PL}(d) \tag{10}$$

in decibels, where P_t is the transmit power, G_t and G_r are the antenna gains at transmitter and receiver side respectively. The path loss is usually modeled over the log-distance in the following:

$$\text{PL}(d) = \text{PL}_0 + 10n\lg(d) + X_\Omega\,(\text{dB}), \tag{11}$$

Table 2: Measurement scenarios and configurations.

Room	Freq. range (GHz)	Antenna (TX/RX)			Denoted
		TX	RX	Height (m)	
A	57 ∼ 59	Omn.	Omn.	1.4/1.4	$\text{OO}_{0.0}$
				1.9/1.4	$\text{OO}_{0.5}$
				2.4/1.4	$\text{OO}_{1.0}$
B	58 ∼ 59	Fan.	Omn.	2.5/1.4	FO
			Fan.		FF, $\text{FF}_{\pm 35^\circ}$
			Pen.		FP, $\text{FP}_{\pm 35^\circ}$

where PL_0 gives the reference path loss at $d = 1$ m, n is the loss exponent, and X_Ω denotes a zero mean Gaussian distributed random variable with a standard deviation Ω. The standard deviation statistically describes the variation with respect to the mean path loss at a distance. Mostly, the model parameters in (11) are empirically derived by linearly fitting the measured path loss in dB over log-distance.

Figure 2 depicts the measured power level at the receiver for various antenna configurations when a unit power (0 dBm) is transmitted. The solid line shows the received power in free space.[2] Note that the abscissa axis is the travel distance of the first arrived wave, that is, the direct wave for the LOS case and the first reflected wave for the NLOS case. In this way, the scattered data can be better fitted by the log-distance model (11), since mostly the first arrived wave will have the most significant contribution to the received power. Apparently, the measured scattered data are widely scattered around the free-space curve for the omnidirectional configurations in Figure 2(a), due to the highly reflective environment. In contrast, for the directive antenna configurations in Figure 2(b), the power levels are much higher and the scattered points strongly follow the free space curve, except those points close to the transmitter that are very sensitive to the (unintentional) beam pointing errors.[3] When the RX beams are misaligned intentionally by ±35° over the boresight, the received power by the Fan-Pen configuration will drop about 25 dB due to narrower antenna beam, compared to the 4 dB drop by the Fan-Fan one. Notice that the 35°-misalignment is about half the beamwidth of the fan-beam antenna and thus the direct path is still within the sight.

By fitting the measured data in Figure 2 to (11), we get the log-distance model parameters listed in Table 3. Here for the case of directive configurations in Figure 2(b), the scattered points within the distance of 2 to 3 meters are not considered during the fittings. It appears that the loss exponents are much smaller than the free-space exponent 2 for the Omn-Omn configurations, but approximately equal to 2 for the directive ones.

[2] The peak antenna gain is taken into account for the calculation of the received power in free space. For the NLOS scenario, the reflection loss over the wall is not taken into account for the calculation of the received power at the travel distance of the first reflected wave.

[3] Notice that for the Fan-Omn case, when the transmitter and receiver are close to each other, the lower signal level is caused by the narrow beamwidth of the omnidirectional antenna in the vertical plane.

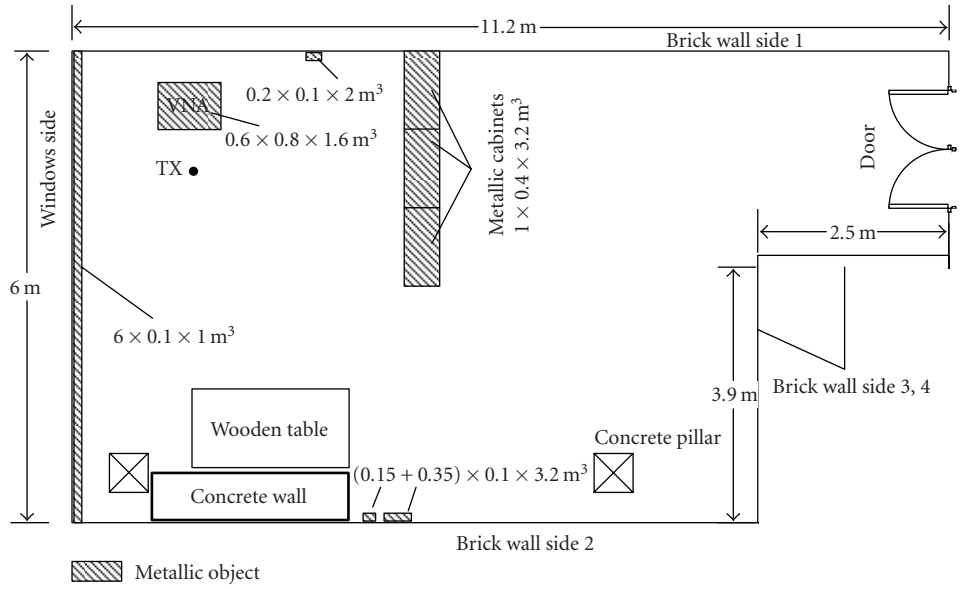

(a) Room A

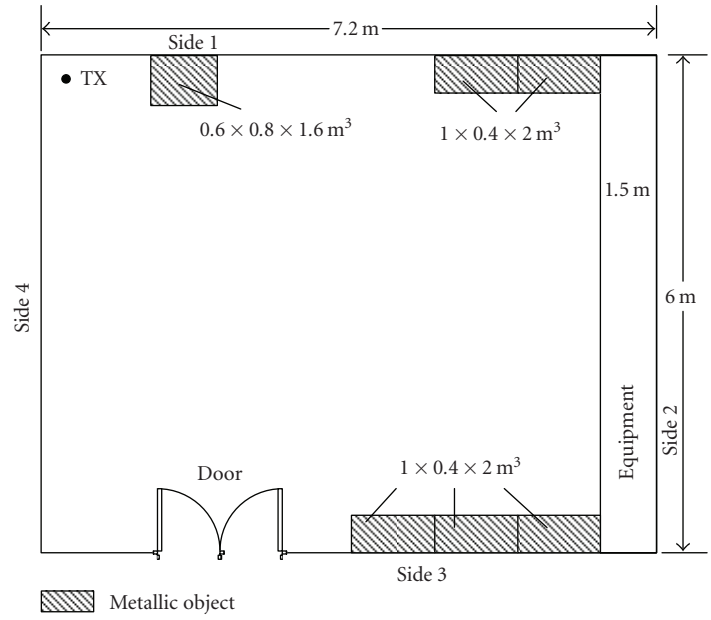

(b) Room B

Figure 1: Plan view of the measured rooms.

3.3. *K*-factor, RDS, and coherence bandwidth

Figures 3 and 4 depict instantaneous K-factors and RMS delay spreads derived from the measured power delay profiles. Figure 4(c) shows a magnified version of Figure 4(b) so that the results can be well distinguished for directive configurations. In addition, we also estimated the coherence bandwidth $B_{c0.5}$ and $B_{c0.9}$ at the correlation level 0.5 and 0.9, respectively, as shown in Figure 5 for $B_{c0.5}$. The mean values of them are listed in Table 3 for each configuration. When calculating a K-factor, the power contributed by the dominant path is derived by adding up the powers within the resolution bin of the dominant path. The RDS is calculated from the delay profile with a dynamic range fixed at 30 dB.

For the directive configurations of Fan-Fan and Fan-Pen, as the result of the significant suppression of multipath waves, it is observed that most of the channel parameters are in the region of $K > 10$, $\sigma_\tau < 1.5$ ns, $B_{c0.5} > 400$ MHz, and $B_{c0.9} > 40$ MHz, respectively. When the TX/RX beams are not pointing to each other, the beam-pointing errors, for example, the 35°-misalignment for the Fan-Pen configuration, can seriously worsen the channel condition in terms of

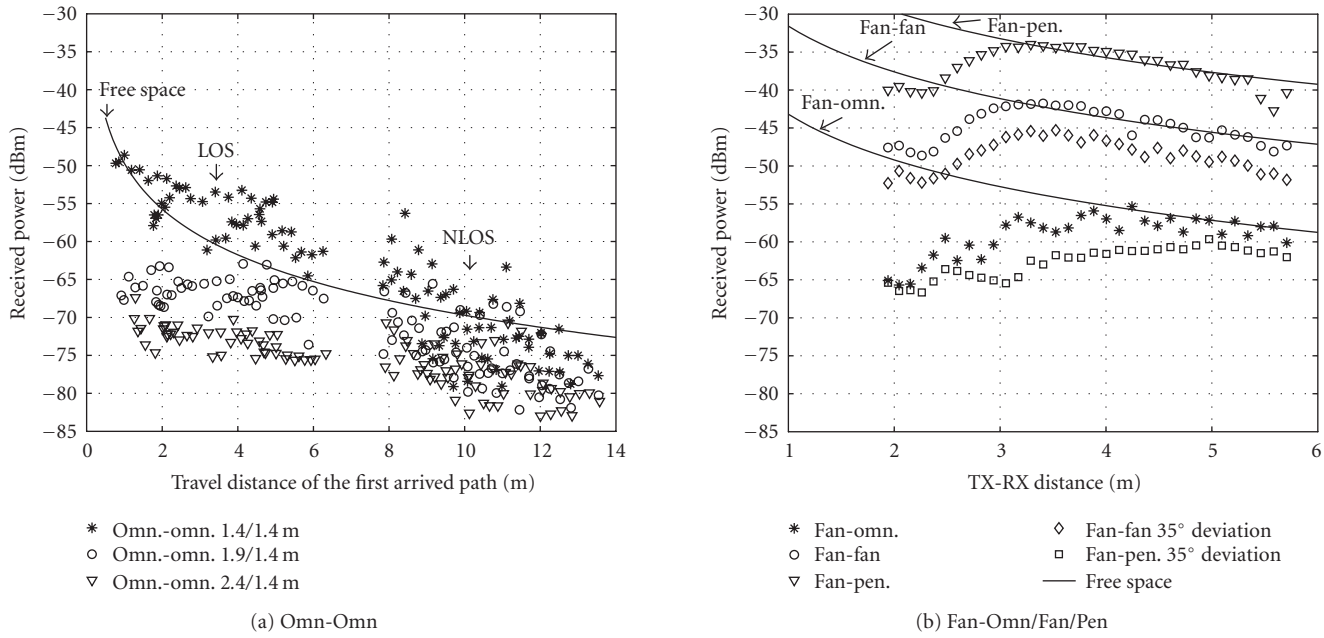

(a) Omn-Omn (b) Fan-Omn/Fan/Pen

Figure 2: The received power over the travel distance of the first arrived path, when the transmit power is 0 dBm.

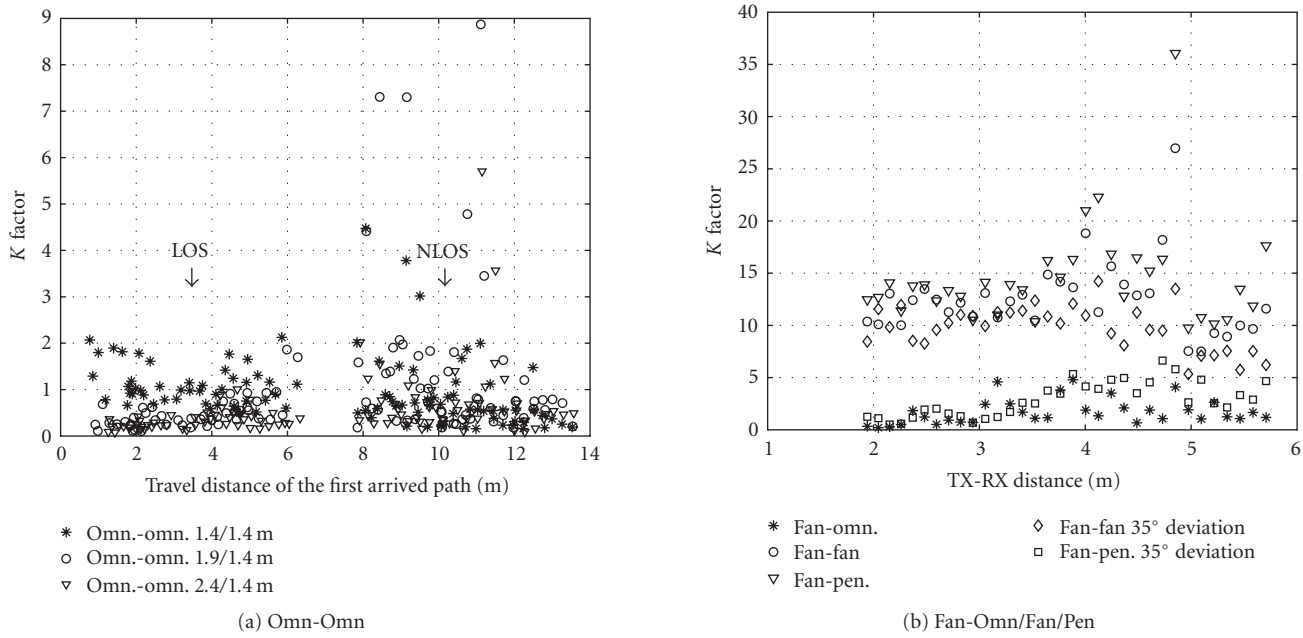

(a) Omn-Omn (b) Fan-Omn/Fan/Pen

Figure 3: The measured instantaneous K-factor over the travel distance of the first arrived path.

large RDSs and the enormous drop of received powers, K-factors, and coherence bandwidth. This implies that channel configurations with wider beams are less sensitive for beam-pointing errors. In this case, the width of the beam has to be properly designed to prevent an enormous drop of channel quality caused by beam-pointing errors. In practice, multiple antennas can be deployed and beamforming algorithms will be used to achieve higher gain and suppress multipath effect by steering the main beam to the direction of the strongest path.

When an omnidirectional antenna is used at TX or RX side, most of the channel parameters are in the region of $K < 3$, $\sigma_\tau > 5$ ns, $B_{c0.5} < 200$ MHz and $B_{c0.9} < 20$ MHz. The K-factors in the LOS case are generally small because of the highly reflective environment. Under the NLOS condition, channel parameters are strongly variant depending on the

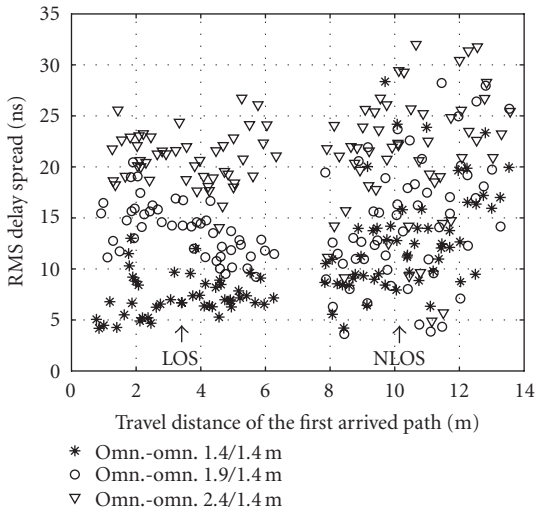

(a) Omn-Omn

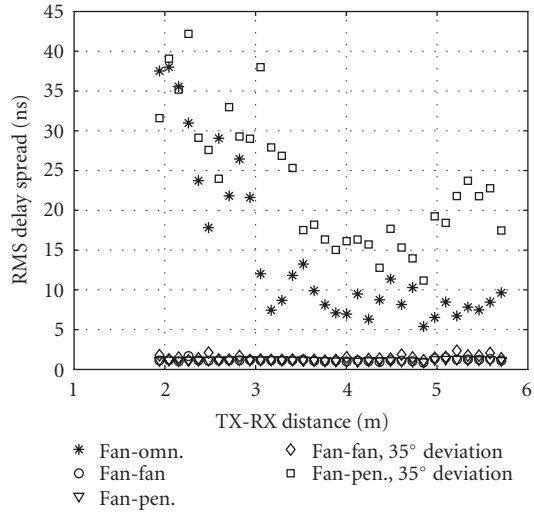

(b) Fan-Omn/Fan/Pen

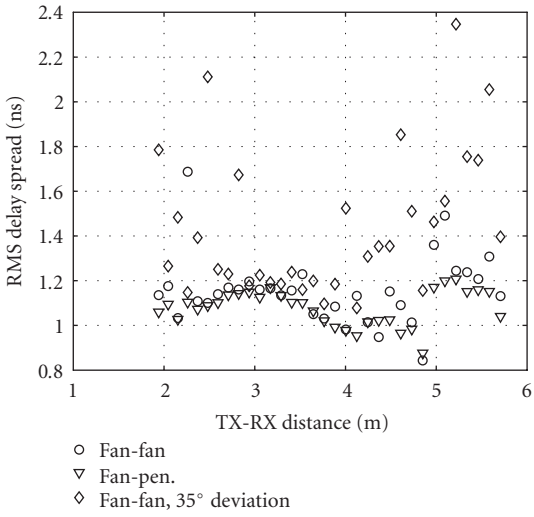

(c) Magnification of Figure 4(b)

Figure 4: The instantaneous RMS delay spread over the travel distance of the first arrived path.

position of the receiver, due to the absence of the direct path. In some NLOS channels, a strong wave reflected from walls appears and leads to desirable values of channel parameters. In particular, the K-factors at some NLOS positions are larger than 4, since the strongest wave reflects at the metallic cable boxes attached to the wall and is much stronger than other reflected waves.

The coherence bandwidth is strongly related to the K-factor and the RDS, which embodies the Fourier transform relationship between the frequency autocorrelation function and the power delay profile described in Section 2. Generally speaking, the larger is the K-factor, the smaller is the RDS and thus the larger is the coherence bandwidth. For a specific shape of the power delay profile, one would expect a fixed relationship between coherence bandwidth and RDS [11]. From the measured data, we have found that for all the antenna configurations the coherence bandwidths at level 0.9 can be empirically related to the RDSs by $\sigma_\tau \cdot B_{c0.9} = 0.063$ [14], but the mean values of $\sigma_\tau \cdot B_{c0.5}$ are highly variant for different configurations.

3.4. Maximum excess delay and number of multipath components

Within the dynamic range of 30 dB of power delay profiles, the maximum excess delay $\tau_{\max}$ and the number of multipath components N are investigated for various measurement configurations. Multipath components are recognized from the local peaks in a profile. The values of $\tau_{\max}$ are distributed in different regions within 10 to 170 nanoseconds and so is the case for the values of N within 3 to 100, depending on the channel configurations. The mean values are summarized in Table 3. Also, the value of N is strongly related to the value of $\tau_{\max}$, that is, the number of multipath components will increase with the maximum excess delay. For all the measured profiles, the number of paths per nanosecond, $N/\tau_{\max}$, has a mean value of 0.30 with a small standard deviation of 0.06. This leads to an empirical relationship $N = \lceil 0.30 \cdot \tau_{\max} \rceil$.

3.5. Power delay profile shape

To investigate the shape of power delay profiles for various channel configurations, we take the average over all the measured profiles for each configuration. Here, each individual measured profile is normalized by its total received power. As an example, Figure 6 depicts the average profiles for the configurations of Omn-Omn and Fan-Pen. From these average profiles, we observe the following.

(i) When the TX/RX beams are aligned to each other under the LOS condition, for example, the cases of Omn-Omn 1.4/1.4 m and Fan-Fan/Pen, the average delay profile consists of a direct ray and an exponentially decaying part.

(ii) In other LOS cases when the TX/RX beams are strongly misaligned and out sight of each other, a constant level part will appear before an exponentially decaying part. The duration of the constant part depends on

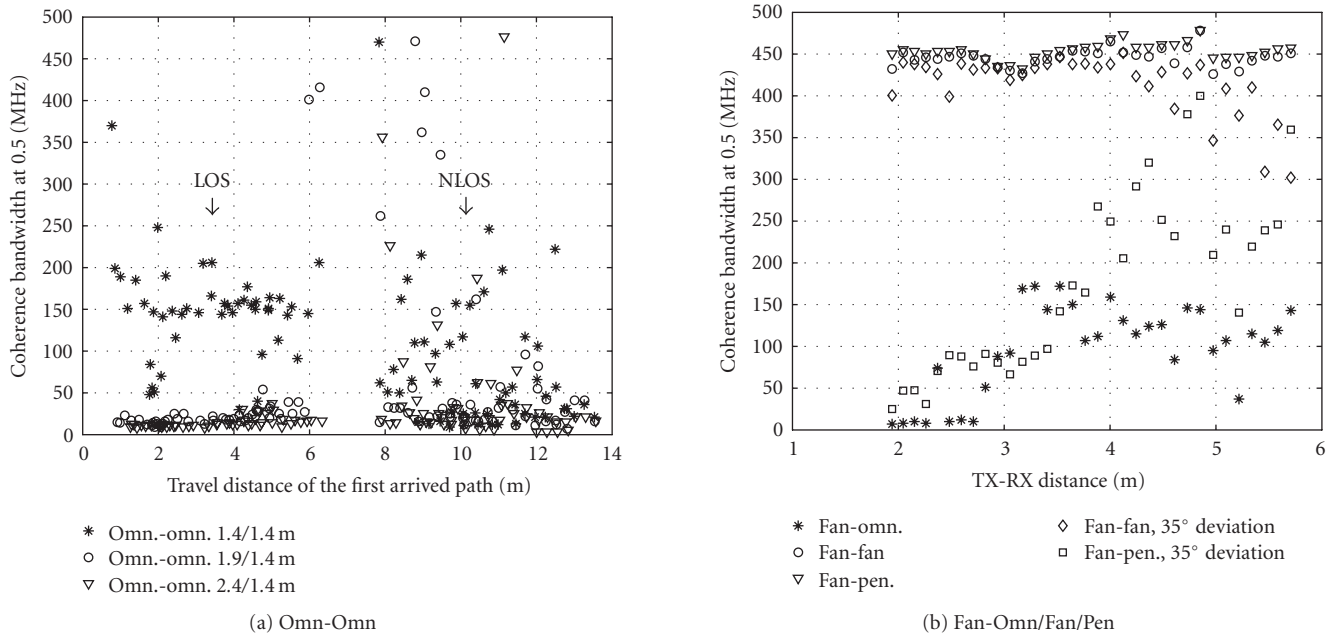

(a) Omn-Omn

(b) Fan-Omn/Fan/Pen

Figure 5: The coherence bandwidth at level 0.5 over the travel distance of the first arrived path.

Table 3: The log-distance model parameters $\{PL_0, n, \Omega\}$, the mean values of K, σ_τ, B_c, τ_{max}, and N for various configurations, and the PDP shape parameters $\{s, \tau_c, \gamma\}$.

Cases	LOS			NLOS			LOS				
	$OO_{0.0}$	$OO_{0.5}$	$OO_{1.0}$	$OO_{0.0}$	$OO_{0.5}$	$OO_{1.0}$	FO	FF	FP	$FF_{\pm 35°}$	$FP_{\pm 35°}$
PL_0 (dB)	68.3	83.8	87.8	34.8	56.7	71	79.7	67.0	67.4	72.2	115
n	1.2	0.2	0.6	5.4	3.8	2.7	0.4	2.1	2.0	1.9	−1.5
Ω (dB)	2.7	2.0	1.3	3.9	3.3	2.7	1.0	0.8	0.6	0.9	0.8
$E\{K\}$	1.1	0.5	0.3	0.9	1.6	0.7	1.7	12.5	14.5	9.8	2.9
$E\{\sigma_\tau\}$ (ns)	7.3	13.8	20.8	12.9	14.8	21.0	14.6	1.2	1.1	1.4	23.3
$E\{B_{c0.5}\}$ (MHz)	155.1	37.6	14.0	108.4	148.2	55.9	95.3	445.9	453.4	414.1	173.0
$E\{B_{c0.9}\}$ (MHz)	15.4	5.6	3.0	6.4	6.5	2.6	6.3	51.8	55.6	44.7	3.2
$E\{\tau_{max}\}$ (ns)	67.8	116.6	144.8	120.6	133.4	146.1	113.2	15.7	15.4	21.5	141.7
$E\{N\}$	20.0	34.0	47.2	35.5	38.6	47.5	28.7	5.0	4.8	5.8	38.3
s (dB)	0	3.3	2.7	0	0	0	3.1	0	0	0	3.3
$E\{\tau_c\}$ (ns)	0	29.5	39.0	0	0	0	27.6	0	0	0	66.7
$E\{\gamma\}$ (dB/ns)	0.2	0.11	0.07	0.07	0.06	0.04	0.14	0.48	0.48	0.42	0.05

the extent of the misalignment and the beam pattern of the antenna.

(iii) In addition, under the NLOS condition, the average delay profile will be exponentially decaying without a constant part, due to the lower dependency of antenna pattern and beam misalignment.

According to the observation, the average delay profile can be modeled as a function of excess delay that consists of a direct ray, a constant part, and a linear decaying part, as shown in Figure 6. This model was first proposed in [21] and further developed in [36]. Mathematically, the power delay profile shape of a Rician channel is modeled by

$$P(\tau) = \begin{cases} 0, & \tau < 0, \\ |\alpha_0|^2 \delta(\tau), & \tau = 0, \\ \Pi, & 0 < \tau \le \tau_c, \\ \Pi \cdot e^{-\gamma(\tau - \tau_c)}, & \tau > \tau_c, \end{cases} \tag{12}$$

where α_0 is the amplitude of the specular path, $\sqrt{\Pi}$ is the amplitude of the constant part with duration τ_c, and $\gamma = (A/10)\ln 10$ is the decay exponent with A in dB/ns. When the

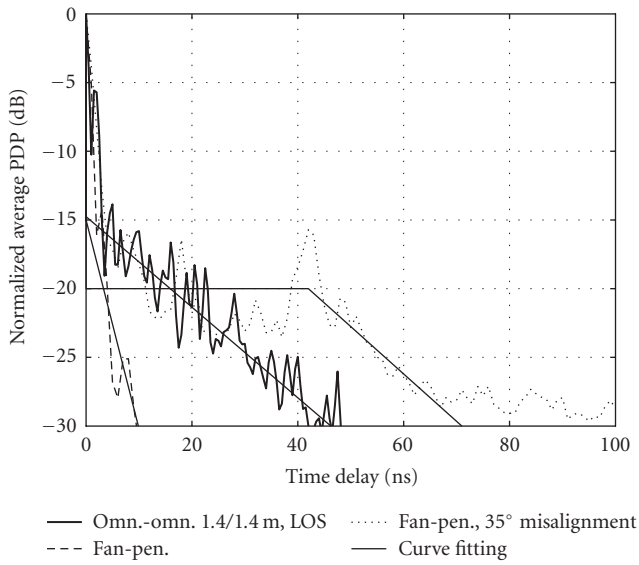

FIGURE 6: Average power delay profiles and curve fittings for the Fan-Omn/Fan/Pen configurations.

constant part disappears, that is, $\tau_c = 0$, it becomes the commonly applied exponentially decaying channel model. Letting $|\alpha_0|^2 = 0$, Rayleigh fading channels are described.

Since the duration τ_c is mainly affected by the narrow-beam antenna pattern and the beam misalignment, and the decay exponent γ is strongly related to a specific environment, particularly the reflection loss of walls, it is reasonable to assume that the product $\tau_c\gamma$ is fixed for a specific antenna configuration in an environment. Based on this assumption, to simplify this model, here we introduce a new parameter $s = \tau_c\gamma$ that defines the shape of a profile. When the shape parameter is known, the channel parameters $\{P, K, \sigma_\tau\}$, where P is the average channel power, can be related to the model parameters $\{|\alpha_0|^2, \Pi, \gamma, \tau_c\}$ as listed in Table 4. In the table, we have $s_1 = s + 1$, $s_2 = s^2/2 + s + 1$ and $s_3 = s^3/3 + s^2 + 2s + 2$.

From the measured results, the shape parameter s can be achieved by fitting the average PDP with (12) for each configuration. Then for each individual measured profile, the model parameters $\{|\alpha_0|^2, \Pi, \gamma, \tau_c\}$ can be retrieved by taking the channel parameters $\{P, K, \sigma_\tau\}$ into the channel-to-model formulas in Table 4. With these model parameters, the channel can be simulated and used for the performance evaluation of a system, as we will see in Section 4. Table 3 lists the shape parameters s and the mean values of the model parameters γ and τ_c for various configurations.

4. SYSTEM DESIGN AND BER PERFORMANCE EVALUATION

In this section, we analyze the link budget for designing a 60 GHz system and performs simulation of an OFDM system. Based on the simulated system, the BER performance is evaluated by using the measured and modeled channels.

4.1. Link budget and scenario analysis

Examining the link budget requirement for a radio system needs to determine the required signal strength at the receiver, that is, receiver sensitivity

$$P_{\mathrm{RX}} = \frac{C}{N} + L_I + N_0\,(\mathrm{dB}), \tag{13}$$

where C/N stands for the required carrier-to-noise ratio for demodulation, L_I is the implementation loss of a transceiver and $N_0 = -174 + 10\lg B + F$ is the thermal noise level in dB at a standard temperature 17° with B the bandwidth in Hz and F the noise figure. By knowing the receiver sensitivity and the received power at a distance d, one can examine the link margin $M = P_r(d) - P_{\mathrm{RX}}$ to see whether the transmitted signal can be recovered properly.

For a coded OFDM system, a certain level of C/N is required in the receiver to achieve a proper demodulation and decoding for different constellations. Here, we take the minimum C/N level in Table 5 required for quasi-error-free reception in Rayleigh channels as a reference.[4] The values are based on comprehensive system simulations and were computed on the assumption that the channel knowledge is perfectly known in the receiver [37]. For the considered OFDM system, the code rate is 3/4 and the guard interval is one-fourth of the useful symbol duration. If $L_I = 2.5$ dB, $B = 1.28$ GHz, and $F = 7$ dB, then one can readily calculate the receiver sensitivities as $P_{\mathrm{RX}} = -62.7, -56.6, -51.5$ dBm for the constellations of QPSK, 16-QAM, and 64-QAM, respectively.

Next we examine possible constellations of the OFDM system for the channel configurations and environments described in Section 3. Given the transmitted power $P_t = 10$ dBm and the TX-RX separation $d = 6$ m, the mean received power $P_r(d)|_{d=6}$ can be predicted from (10) and the link margin can be determined. Table 5 lists the feasibility of the constellations for the LOS channels. In particular, for directive configurations, as long as the TX-RX beams are well aligned, the link margin is always larger than zero within a range of 6 meters for the three constellations and thus the channel bit rate up to 6 Gbps can be achieved. Actually, for the Fan-Fan and Fan-Pen configurations, the remaining link margins allow the radio coverage to be further extended. For the omnidirectional configuration with TX-RX antennas at the same height, the channel bit rate up to 4 Gbps is achievable by using 16-QAM. Additionally, by using QPSK to examine the NLOS channels, we observe that only half of the NLOS area can be covered by omnidirectional antennas. One would expect that the shadowing area can be fully covered if high gain directive antennas are applied.

[4] Quasi-error-free reception means in the concatenated coding scheme Viterbi/Reed-Solomon, the bit-error-rate BER = 2×10^{-4} after Viterbi decoding and BER = 10^{-11} after Reed-Solomon decoding [37].

Table 4: Relation between model and channel parameters when the shape parameter s is known (see [36]).

model → channel		channel → model	
$s = \tau_c\gamma \in [0, \infty)$	$s = 0$	$s = \tau_c\gamma$	$s = 0$
$P = \lvert\alpha_0\rvert^2 + \dfrac{\Pi}{\gamma}s_1$	$P = \lvert\alpha_0\rvert^2 + \dfrac{\Pi}{\gamma}$	$\lvert\alpha_0\rvert^2 = P\dfrac{K}{K+1}$	$\lvert\alpha_0\rvert^2 = P\dfrac{K}{K+1}$
$K = \dfrac{\lvert\alpha_0\rvert^2\gamma}{\Pi s_1}$	$K = \dfrac{\lvert\alpha_0\rvert^2\gamma}{\Pi}$	$\gamma = \dfrac{1}{\sigma_\tau}\sqrt{\dfrac{1}{K+1}\dfrac{s_3}{s_1} - \dfrac{1}{(K+1)^2}\dfrac{s_2^2}{s_1^2}}$	$\gamma = \dfrac{1}{\sigma_\tau}\dfrac{\sqrt{2K+1}}{K+1}$
$\sigma_\tau = \dfrac{1}{\gamma}\sqrt{\dfrac{1}{K+1}\dfrac{s_3}{s_1} - \dfrac{1}{(K+1)^2}\dfrac{s_2^2}{u_1^2}}$	$\sigma_\tau = \dfrac{1}{\gamma}\dfrac{\sqrt{2K+1}}{K+1}$	$\Pi = \dfrac{P}{K+1}\dfrac{\gamma}{s_1}$	$\Pi = \dfrac{P}{K+1}\gamma$

Table 5: The required C/N and RX sensitivity for the 3/4 coded OFDM system with guard interval 1/4; the feasibility of modulation schemes for various configurations at a distance $d = 6$ meter in the LOS environments ($\surd$: yes; $\times$: no).

	QPSK	16-QAM	64-QAM
Minimum required C/N (dB)	10.7	16.7	21.7
RX sensitivity (dBm)	−62.7	−56.5	−51.5
Channel bit rate (Gbps)	2.0	4.0	6.0
Information bit rate (Gbps)	1.5	3.0	4.5
$OO_{0.0}$	$\surd$	$\surd$	$\times$
$OO_{0.5}$	$\surd$	$\times$	$\times$
$OO_{1.0}$	$\times$	$\times$	$\times$
FO, FF, FP, $FF_{\pm 35}$, $FP_{\pm 35}$	$\surd$	$\surd$	$\surd$

4.2. Baseband design and simulation of an OFDM system

To analyze the system performance of various channel configurations and evaluate the channel model (12) for the high data rate transmission, we simulate a coded OFDM system by using the measured and modeled channels. The baseband OFDM transmission scheme is depicted in Figure 7 and the system parameters are listed in Table 6. Before mapping to the QPSK symbols in the transmitter, the sequence of user bits undergos a 3/4 convolutional punctured encoder and then a random interleaver in bit level. With the modulation of QPSK and the IFFT/FFT length of 1024, the coded data rate can reach 2 Gbps which is the target rate proposed by the IEEE 802.15.3c task group [5]. Here, the subcarrier spacing is 1.25 MHz and the guard interval is set to be 200 nanoseconds, which are large enough to prevent the possible inter-carrier-interference (ICI) caused by nonlinearities of the RF-frontend and to absorb the ISI between blocks caused by the multipath channel, respectively.

During the baseband simulation, the radio channels are implemented either by the measured impulse responses or the modeled impulse responses according to the delay profile model (12). For the modeled channels, the channel parameters of an individual realization, including K-factor, RDS, the shape parameter s, and the model parameters $\{|\alpha_0|^2, \Pi, \gamma, \tau_c\}$, are the same as those from the measured channels. Note that each delay profile is normalized to have a unit power. Additionally, the transmitter and the receiver

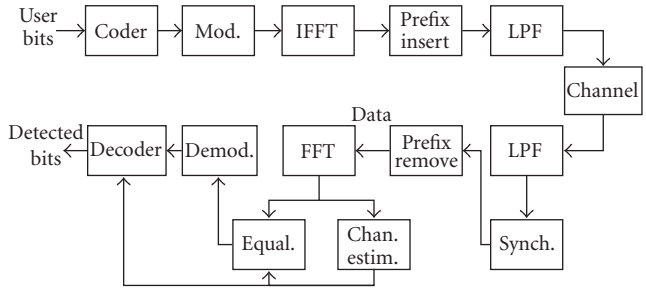

Figure 7: Baseband structure of a coded OFDM system.

Table 6: OFDM system parameters.

Carrier frequency	60 GHz
Modulation scheme	QPSK
Object moving speed	3 m/s
Channel bandwidth	1.28 GHz
Subcarrier number	1024
Subcarrier spacing	1.25 MHz
OFDM symbol duration	800 ns
Guard interval	200 ns
Code rate	3/4
Channel bit rate	2 Gbps
Information bit rate	1.5 Gbps

are considered to be stationary. But the time variation of the channel is caused by one moving object at speed 3 m/s and simulated according to the model (9). In the receiver, additive white Gaussian noise (AWGN) is added to the received signal. The nonlinearity effects, such as phase noise and IQ imbalance caused by the RF-frontend, are not included in the simulation.

In the receiver, for the purpose of time synchronization, the received signal is correlated with a known training symbol to find the best starting point of an OFDM symbol. The training symbol is also used for the zero-forcing estimation of the channel response, which is applied for the one-tap symbol equalization before demodulation. The demodulator outputs the bitwise log-likelihood values for the alphabet of QPSK symbols, which are then used for the soft-decision

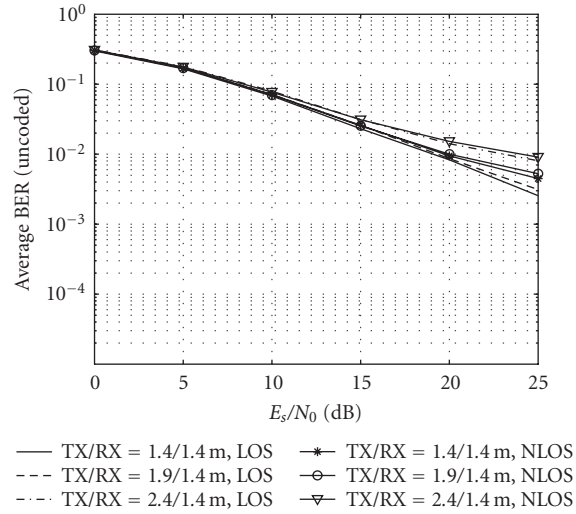

(a) Measured Omn-Omn channels

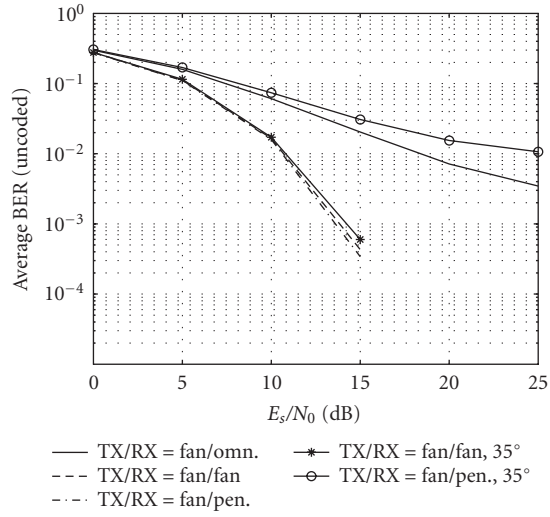

(b) Measured Fan-Omn/Fan/Pen channels

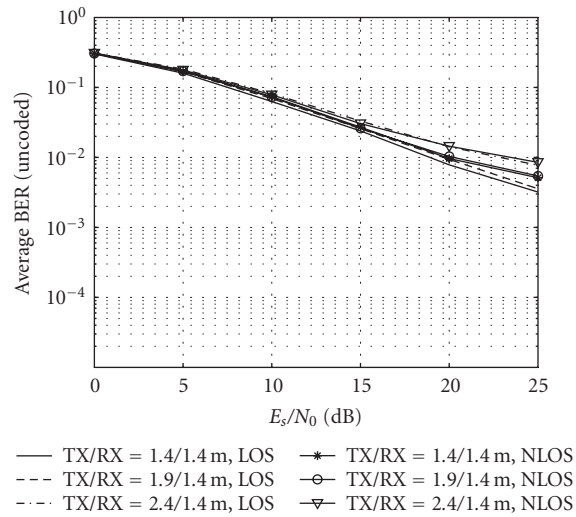

(c) Modeled Omn-Omn channels

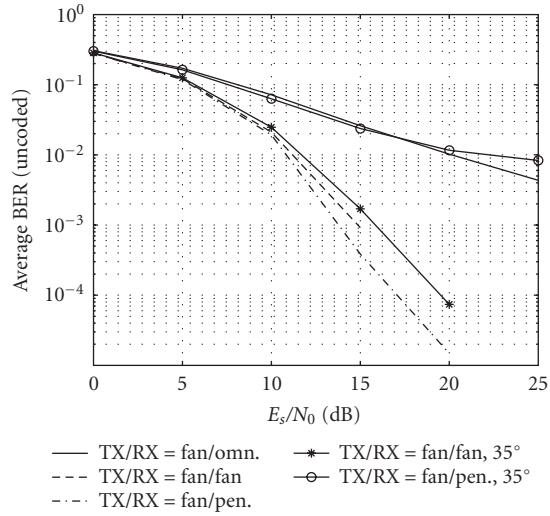

(d) Modeled Fan-Omn/Fan/Pen channels

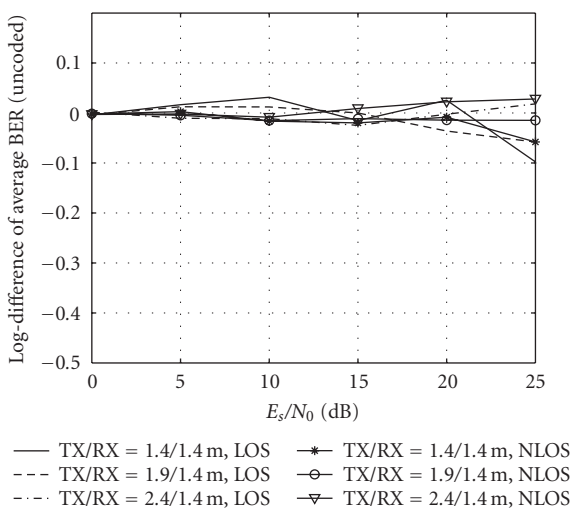

(e) Omn-Omn channels

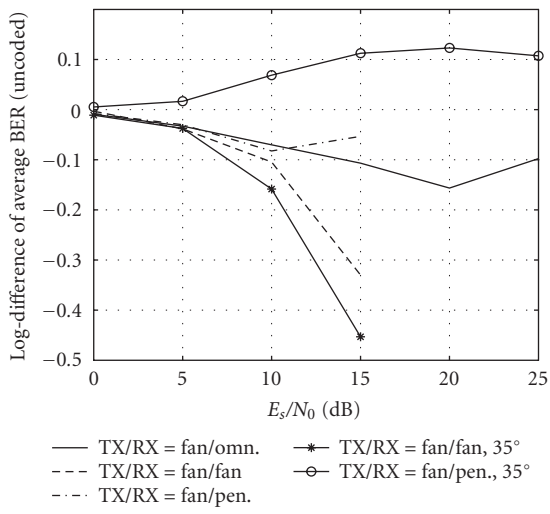

(f) Fan-Omn/Fan/Pen channels

Figure 8: BER performance of uncoded OFDM system based on the measured and modeled channels and the log-difference of average BER between them.

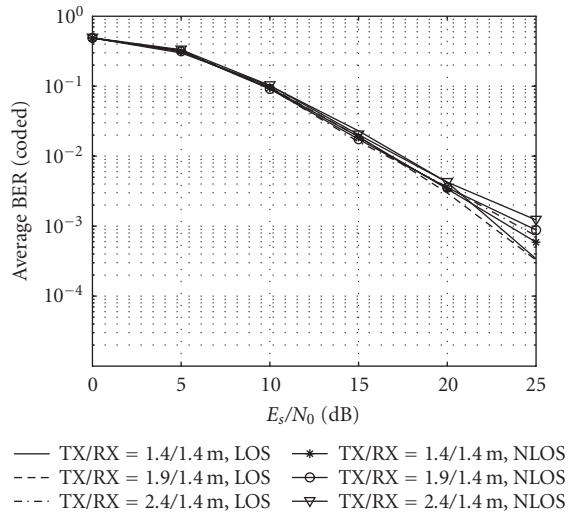

(a) Measured Omn-Omn channels

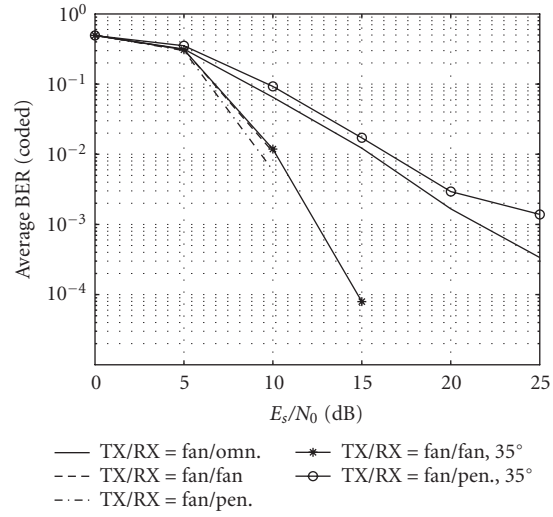

(b) Measured Fan-Omn/Fan/Pen channels

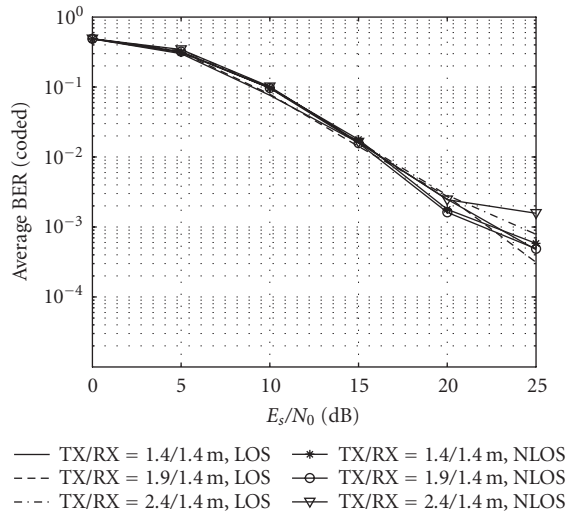

(c) Modeled Omn-Omn channels

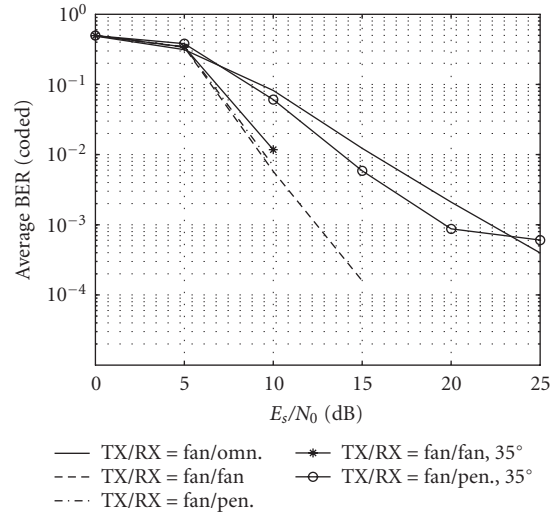

(d) Modeled Fan-Omn/Fan/Pen channels

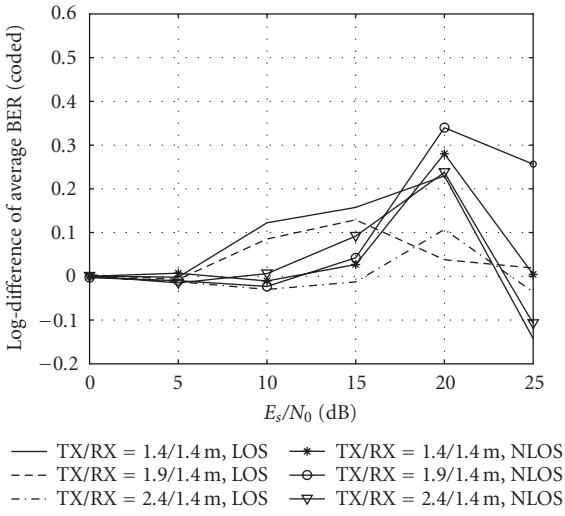

(e) Omn-Omn channels

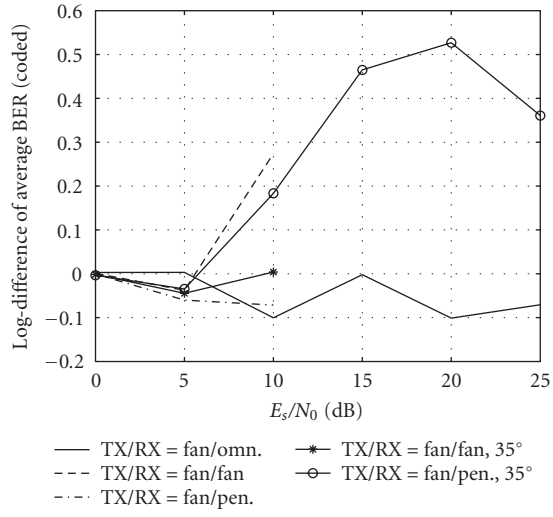

(f) Fan-Omn/Fan/Pen channels

Figure 9: BER performance of coded OFDM system based on the measured and modeled channels and the log-difference of average BER between them.

Viterbi decoding. The simple channel estimation and equalization applied here are sufficient for a low-cost and low-complexity implementation of a 60 GHz system. There is no doubt that the system performance can be further improved by doing better channel estimation and equalization, which however will increase the implementation complexity.

4.3. BER performance analysis

The OFDM system described in Table 6 with and without coding is simulated and the BER performance is evaluated by using the measured and modeled channel impulse responses. For each set of model parameters $\{|\alpha_0|^2, \Pi, \gamma, \tau_c\}$, we conduct 200 runs of simulation.

Figures 8 and 9 depict the average uncoded- and coded-BER performance, respectively, over the receive *C/N* in terms of E_s/N_0 (energy per symbol divided by the noise density). In addition, the difference of average BER in logarithm domain between the measured and modeled channels is also shown in the figures for each antenna configuration. The BER performance is an average over the set of the possible channel responses with a specific TX/RX antenna configuration in one room. At high *C/N*, the BER event might be not well observed due to a limited number of sent bits, particularly for the directive channels, but this would not affect our analysis.

First of all, we observe that the log-differences of average BERs are in the ranges of $[-0.5, 0.1]$ and $[-0.1, 0.5]$ for the uncoded and coded performance, respectively. The small BER differences indicate that the BER curves show a similar performances for the measured and modeled channels for most antenna configurations. It is also important to notice that the modeled channels of Fan/Pen 35° show a more optimistic behavior than the measured ones in the uncoded- and coded-BER performance. This might be caused by the strong cluster behavior in the power delay profile as shown in Figure 6, which is not included in the single-cluster model (12). From these observations, we conclude that the statistical delay profile models according to (12) are well behaved and thus sufficient to evaluate the system performance for various channel configurations, as long as the channel does not show a strong multiple-cluster behavior.

Next for the uncoded BER performance, the Fan-Fan and Fan-Pen configurations achieve a similar performance if the TX-RX beams are well aligned to each other, due to similar channel characteristics as seen in Section 3, and the required *C/N* at BER $= 1 \times 10^{-3}$ is about 15 dB less than the omnidirectional ones. The big gap can be explained by the fact that the time dispersion and frequency selectivity of the directive channels are much less severer than the omnidirectional channels, as seen from Figures 3–5. However, when the RX beam is misaligned about 35° over the boresight, the resulting performance of Fan-Pen channels becomes rapidly worse compared to the slight performance drop of the Fan-Fan ones, which is consistent with the enormous difference between the values of their channel parameters.

With the convolutional coding, interleaving and Viterbi decoding applied in the system, the performance is dramatically improved for omnidirectional channels compared to the lower improvement for the directive channels. This arises because the strong frequency selectivity of omnidirectional channels provides the frequency diversity to the channel, which is exploited by the decoder for error correction with the help of the interleaver. Even so, the coding gain cannot bring the system in the omnidirectional channel to a comparable performance level as in the directive ones. For instance, the Omn-Omn configuration requires at least 10 dB higher signal level than the Fan-Fan one to achieve the same BER $= 1 \times 10^{-3}$. In other words, the directive configurations will save many dBs for the link budget requirement.

In the above BER analysis, all the channels are assumed to have the same received power at each *C/N*. However, for physical channels, the actual received power in Figure 2 and thus the actual *C/N* of each configuration will be different from each other. Taking the actual *C/N* into account in the BER comparison, the directive configurations will further outperform the omnidirectional configurations.

5. CONCLUSIONS

In this paper, we analyzed the time dispersion and frequency selectivity of 60 GHz channels with various antenna configurations based on extensive channel measurements in LOS/NLOS environments. Statistical channel parameters were retrieved from measurements and compared. Particularly, the shape parameters of power delay profiles were retrieved based on a simple profile model. Next the link budget was analyzed and examined for an OFDM system with different constellations and then a baseband OFDM system was simulated to evaluate the BER performance. For the considered environments and antenna configurations, the following conclusions can be drawn from this work.

(i) The link budget analysis shows that directive configurations will provide sufficient link margins and radio coverage for high data rate communications. In this work, the Fan-Fan and Fan-Pen configurations can achieve the data rate of at least 6 Gbps within a range of 6 meters for LOS scenarios, while the Omn-Omn will achieve up to 4 Gbps. It is also preferable to use directive configurations in NLOS scenarios.

(ii) For each channel configuration, the coded/uncoded BER performance agreed well for the measured and modeled channels. This confirms that the simple model of the delay profile shape and its parameters are sufficiently accurate for the evaluation of system performance for various channel configurations without a strong cluster-behavior in the channel.

(iii) Since the multipath effect has been effectively suppressed, a remarkable BER performance is achieved by directive configurations and this leads to the saving of link budget as high as 10 dB compared to omnidirectional ones. Although the omnidirectional configurations can attain higher coding gain from frequency selectivity, the required *C/N* level is still too high to achieve the target BER in practice.

(iv) The TX-RX antenna beams have to be properly aligned within the sight of each other, otherwise the

beam-pointing errors will cause an enormous drop in the channel quality and BER performance. The wider beam antennas are generally less sensitive for beam-pointing errors, which indicates that a proper beamwidth has to be designed in practice.

REFERENCES

[1] M. Fiacco, M. Parks, H. Radi, and S. R. Saunders, "Final report—indoor propagation factors at 17 and 60GHz," Tech. Rep., University of Surrey, Guildford, Surrey, UK, August 1998, study carried out on behalf of the Radiocommunications Agency.

[2] J. Schöthier, "WP3-study: the 60 GHz channel and its modelling," Tech. Rep., 2001, IST-2001-32686 Broadway.

[3] P. F. M. Smulders, "Exploiting the 60 GHz band for local wireless multimedia access: prospects and future directions," *IEEE Communications Magazine*, vol. 40, no. 1, pp. 140–147, 2002.

[4] H. Xu, V. Kukshya, and T. S. Rappaport, "Spatial and temporal characteristics of 60-GHZ indoor channels," *IEEE Journal on Selected Areas in Communications*, vol. 20, no. 3, pp. 620–630, 2002.

[5] IEEE 802.15 WPAN Millimeter Wave Alternative PHY Task Group 3c (TG3c), http://www.ieee802.org/15/pub/TG3c.html.

[6] R. Davies, M. Bensebti, M. A. Beach, and J. P. McGeehan, "Wireless propagation measurements in indoor multipath environments at 1.7 GHz and 60 GHz for small cell systems," in *Proceedings of the 41st IEEE Vehicular Technology Conference (VTC '91)*, pp. 589–593, Saint Louis, Mo, USA, May 1991.

[7] C. R. Anderson, T. S. Rappaport, K. Bae, et al., "In-building wideband multipath characteristics at 2.5 & 60 GHz," in *Proceedings of the 56th IEEE Vehicular Technology Conference (VTC '02)*, vol. 1, pp. 97–101, Vancouver, BC, Canada, September 2002.

[8] R. J. C. Bultitude, R. F. Hahn, and R. J. Davies, "Propagation considerations for the design of an indoor broad-band communications system at EHF," *IEEE Transactions on Vehicular Technology*, vol. 47, no. 1, pp. 235–245, 1998.

[9] N. Moraitis and P. Constantinou, "Indoor channel measurements and characterization at 60 GHz for wireless local area network applications," *IEEE Transactions on Antennas and Propagation*, vol. 52, no. 12, pp. 3180–3189, 2004.

[10] S. Collonge, G. Zaharia, and G. El Zein, "Influence of the human activity on wide-band characteristics of the 60 GHz indoor radio channel," *IEEE Transactions on Wireless Communications*, vol. 3, no. 6, pp. 2396–2406, 2004.

[11] D. C. Cox and R. P. Leck, "Correlation bandwidth and delay spread multipath propagation statistics for 910-MHz urban mobile radio channels," *IEEE Transactions on Communications*, vol. 23, no. 11, pp. 1271–1280, 1975.

[12] B. Glance and L. J. Greenstein, "Frequency-selective fading effects in digital mobile radio with diversity combining," *IEEE Transactions on Communications*, vol. 31, no. 9, pp. 1085–1094, 1983.

[13] H. Hashemi, "The indoor radio propagation channel," *Proceedings of the IEEE*, vol. 81, no. 7, pp. 943–968, 1993.

[14] H. Yang, M. H. A. J. Herben, and P. F. M. Smulders, "Frequency selectivity of 60-GHz LOS and NLOS Indoor Radio Channels," in *Proceedings of the 63rd IEEE Vehicular Technology Conference (VTC '06)*, vol. 6, pp. 2727–2731, Melbourne, Australia, May 2006.

[15] A. A. M. Saleh and R. A. Valenzuela, "A statistical model for indoor multipath propagation," *IEEE Journal on Selected Areas in Communications*, vol. 5, no. 2, pp. 128–137, 1987.

[16] Q. H. Spencer, B. D. Jeffs, M. A. Jensen, and A. L. Swindlehurst, "Modeling the statistical time and angle of arrival characteristics of an indoor multipath channel," *IEEE Journal on Selected Areas in Communications*, vol. 18, no. 3, pp. 347–360, 2000.

[17] C.-C. Chong, C.-M. Tan, D. I. Laurenson, S. McLaughlin, M. A. Beach, and A. R. Nix, "A new statistical wideband spatio-temporal channel model for 5-GHz band WLAN systems," *IEEE Journal on Selected Areas in Communications*, vol. 21, no. 2, pp. 139–150, 2003.

[18] C.-C. Chong and S. K. Yong, "A generic statistical-based UWB channel model for high-rise apartments," *IEEE Transactions on Antennas and Propagation*, vol. 53, no. 8, part 1, pp. 2389–2399, 2005.

[19] A. F. Molisch, D. Cassioli, C.-C. Chong, et al., "A comprehensive standardized model for ultrawideband propagation channels," *IEEE Transactions on Antennas and Propagation*, vol. 54, no. 11, part 1, pp. 3151–3166, 2006.

[20] H. Takai, "In-room transmission BER performance of anti-multipath modulation PSK-VP," *IEEE Transactions on Vehicular Technology*, vol. 42, no. 2, pp. 177–185, 1993.

[21] P. F. M. Smulders, "Broadband wireless LANs: a feasibility study," Ph.D. dissertation, Eindhoven University of Technology, Eindhoven, The Netherlandss, December 1995.

[22] J. C.-I. Chuang, "The effects of time delay spread on portable radio communications channels with digital modulation," *IEEE Journal on Selected Areas in Communications*, vol. 5, no. 5, pp. 879–889, 1987.

[23] F. Adachi and K. Ohno, "BER performance of QDPSK with postdetection diversity reception in mobile radio channels," *IEEE Transactions on Vehicular Technology*, vol. 40, no. 1, part 2, pp. 237–249, 1991.

[24] L. Dossi, G. Tartara, and F. Tallone, "Statistical analysis of measured impulse response functions of 2.0 GHz indoor radio channels," *IEEE Journal on Selected Areas in Communications*, vol. 14, no. 3, pp. 405–410, 1996.

[25] J. B. Andersen, T. S. Rappaport, and S. Yoshida, "Propagation measurements and models for wireless communications channels," *IEEE Communications Magazine*, vol. 33, no. 1, pp. 42–49, 1995.

[26] J. Medbo, H. Hallenberg, and J.-E. Berg, "Propagation characteristics at 5 GHz in typical radio-LAN scenarios," in *Proceedings of the 49th IEEE Vehicular Technology Conference (VTC '99)*, vol. 1, pp. 185–189, Houston, Tex, USA, May 1999.

[27] P. A. Bello, "Characterization of randomly time-variant linear channels," *IEEE Transactions on Communications Systems*, vol. 11, no. 4, pp. 360–393, 1963.

[28] P. Marinier, G. Y. Delisle, and C. L. Despins, "Temporal variations of the indoor wireless millimeter-wave channel," *IEEE Transactions on Antennas and Propagation*, vol. 46, no. 6, pp. 928–934, 1998.

[29] G. Durgin, T. S. Rappaport, and H. Xu, "Measurements and models for radio path loss and penetration loss in and around homes and trees at 5.85 GHz," *IEEE Transactions on Communications*, vol. 46, no. 11, pp. 1484–1496, 1998.

[30] R. H. Clarke, "A statistical theory of mobile-radio reception," *Bell System Technical Journal*, vol. 47, no. 6, pp. 957–1000, 1968.

[31] W. C. Jakes, *Microwave Mobile Communications*, John Wiley & Sons, New York, NY, USA, 1974.

[32] T. Aulin, "A modified model for the fading signal at a mobile radio channel," *IEEE Transactions on Vehicular Technology*, vol. 28, no. 3, pp. 182–203, 1979.

[33] S. Qu and T. Yeap, "A three-dimensional scattering model for fading channels in land mobile environment," *IEEE Transactions on Vehicular Technology*, vol. 48, no. 3, pp. 765–781, 1999.

[34] S. Thoen, L. Van der Perre, and M. Engels, "Modeling the channel time-variance for fixed wireless communications," *IEEE Communications Letters*, vol. 6, no. 8, pp. 331–333, 2002.

[35] K. Sato and T. Manabe, "Estimation of propagation-path visibility for indoor wireless LAN systems under shadowing condition by human bodies," in *Proceedings of the 48th IEEE Vehicular Technology Conference (VTC '98)*, vol. 3, pp. 2109–2113, Ottawa, Canada, May 1998.

[36] K. Witrisal, G. Landman, and A. Bohdanowicz, "Practical application of a novel method for estimating the RMS delay spread from power measurements," in *Proceedings of the 4th European Mobile Communications Conference (EPMCC '01)*, Vienna, Austria, February 2001.

[37] ETSI, "Digital Video Broadcasting (DVB); framing structure, channel coding and modulation for digital terrestrial television," European Telecommunications Standards Institute, November 2004, eN 300 744 V1.5.1.

EURASIP JOURNAL ON ADVANCES IN SIGNAL PROCESSING

Special Issue on
Machine Learning in Image Processing

Call for Papers

Images have always played an important role in human life since vision probably is human beings' most important sense. As a consequence, the field of image processing has numerous applications (medical, military, etc.). Nowadays and more than ever, images are everywhere and it is very easy for everyone to generate a huge amount of images thanks to the advances in digital technologies. With such a profusion of images, traditional image processing techniques have to cope with more complex problems and have to face with their adaptability according to human vision. Vision being complex, machine learning has emerged as a key component of intelligent computer vision programs when adaptation is needed (e.g., face recognition) . Among the existing methods, one can quote neural networks, hidden Markov models, kernel based methods, and so forth. However, this mainly concerns the computer vision field, the learning of which emulates high-level vision processes (e.g., visual information categorization or interpretation). But one can also incorporate learning in image processing to emulate low-level vision processes. We can quote edge detection, noise filtering, adaptive compression, and so on, as such potential issues. With the advent of image datasets and benchmarks, machine learning and image processing have recently received a lot of attention. An innovative integration of machine learning in image processing is very likely to have a great benefit to the field, which will contribute to a better understanding of complex images. The number of image processing algorithms that incorporate some learning components is expected to increase, as adaptation is needed. However, an increase in adaptation is often linked to an increase in complexity and one has to efficiently control any machine learning technique to properly adapt it to image processing problems. Indeed, processing huge amounts of images means being able to process huge quantities of data often of high dimensions, which is problematic for most machine learning techniques. Therefore, an interaction with the image data and with image priors is necessary to drive model selection strategies.

The primary purpose of this special issue is to increase the awareness of image processing researchers to the impact of machine learning algorithms in low-level tasks. Papers submitted to this special issue have to carefully address the problem of model selection (features selection, parameter or hyperparameters estimation) for the machine learning technique under consideration.

This special issue aims at providing original and high-quality submissions related, but not limited, to one or more of the following topics:

- Machine learning in image filtering
- Machine learning in image restoration
- Machine learning in edge detection
- Machine learning in image feature extraction
- Machine learning in image segmentation
- Machine learning in image compression
- Machine learning driven by imaging applications.

Moreover, since image databases created for benchmarking or for training are crucial for progress in both machine learning and image processing fields, the evaluation of the submitted papers will take that aspect into account (accessibility, quality, reproducibility) and the performance evaluation has to be carefully adressed.

Authors should follow the EURASIP Journal on Advances in Signal Processing manuscript format described at the journal site http://www.hindawi.com/journals/asp/. Prospective authors should submit an electronic copy of their complete manuscript through the journal Manuscript Tracking System at http://mts.hindawi.com/ according to the following timetable:

Manuscript Due	October 1, 2007
First Round of Reviews	December 1, 2007
Publication Date	March 1, 2008

Guest Editors:

Olivier Lezoray, Vision and Image Analysis (VAI) Team, Cherbourg Applied Sciences University Laboratory (LUSAC), 120 Rue de l'Exode, 50000 Saint-Lô, France; olivier.lezoray@unicaen.fr

Christophe Charrier, Vision and Image Analysis (VAI) Team, Cherbourg Applied Sciences University Laboratory (LUSAC), 120 Rue de l'Exode, 50000 Saint-Lô, France; christophe.charrier@unicaen.fr

Hubert Cardot, Pattern Recognition and Image Analysis Team, Computer Science Laboratory (LI), Université François Rabelais de Tours, 64 avenue Jean Portalis, 37200 Tours, France; hubert.cardot@univ-tours.fr

Sébastien Lefèvre, Models Images Vision (MIV) Team, Image Sciences, Computer Sciences and Remote Sensing Laboratory (LSIIT), CNRS and Louis Pasteur University (Strasbourg), Pôle API, Bd. Brant, BP 10413, 67412 Illkirch, France; lefevre@lsiit.u-strasbg.fr

Hindawi Publishing Corporation
http://www.hindawi.com

EURASIP Book Series on Signal Processing and Communications

UWB Communication Systems—A Comprehensive Overview

Edited by: Maria-Gabriella Di Benedetto,
Thomas Kaiser, Andreas F.Molisch, Ian Oppermann,
Christian Politano, and Domenico Porcino

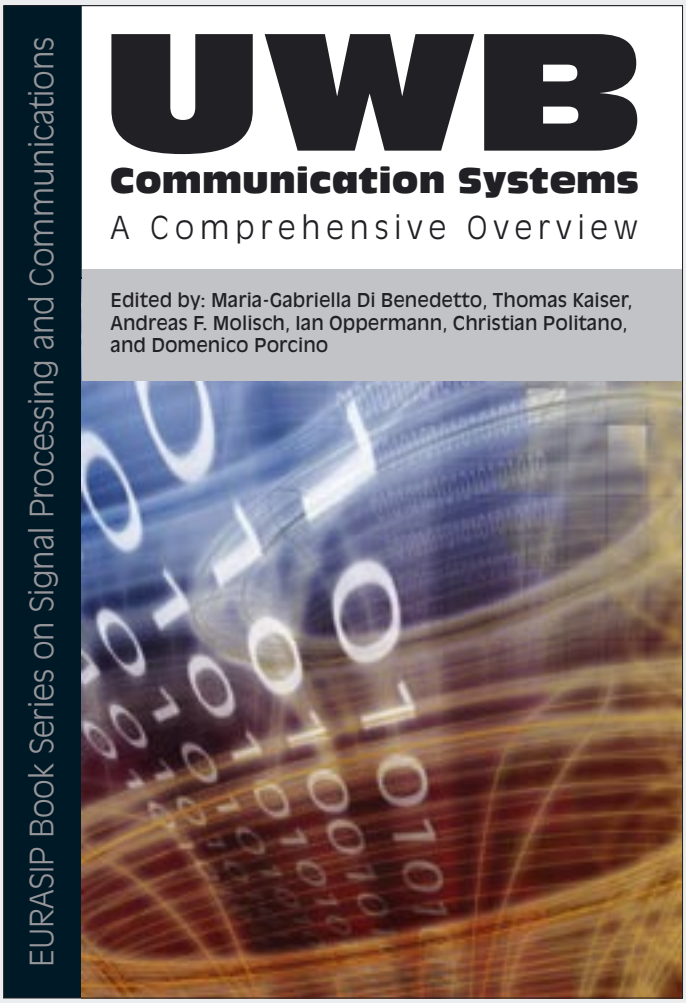

Ultrawideband (UWB) communication systems offer an unprecedented opportunity to impact the future communication world. The enormous available bandwidth, the wide scope of the data rate / range trade-off, as well as the potential for very low-cost operation leading to pervasive usage, all present a unique opportunity for UWB systems to impact the way people and intelligent machines communicate and interact with their environment.

The aim of this book is to provide an overview of the state of the art of UWB systems from theory to applications. Due to the rapid progress of multidisciplinary UWB research, such an overview can only be achieved by combining the areas of expertise of several scientists in the field. More than 30 leading UWB researchers and practitioners have contributed to this book covering the major topics relevant to UWB. These topics include UWB signal processing, UWB channel measurement and modeling, higher-layer protocol issues, spatial aspects of UWB signaling, UWB regulation and standardization, implementation issues, and UWB applications as well as positioning.

The book is targeted at advanced academic researchers, wireless designers, and graduate students wishing to greatly enhance their knowledge of all aspects of UWB systems.

EURASIP Book Series on SP&C, Volume 5, ISBN 977-5945-10-0
Please visit http://www.hindawi.com/spc.5.html for more information about the book. To place an order while taking advantage of our current promotional offer, please contact books.orders@hindawi.com